



## Article

# Induction Generator with Direct Control and a Limited Number of Measurements on the Side of the Converter Connected to the Power Grid

Andrzej Bogdan Kasprawicz <sup>1,\*</sup>, Oleksandr Husev <sup>2</sup> and Ryszard Strzelecki <sup>3,\*</sup><sup>1</sup> Faculty of Electrical Engineering, Gdynia Maritime University, 81-225 Gdynia, Poland<sup>2</sup> Department of Electrical Power Engineering and Mechatronics, Tallinn University of Technology, 19086 Tallinn, Estonia<sup>3</sup> Faculty of Electrical and Control Engineering, Gdańsk University of Technology, 80-233 Gdańsk, Poland

\* Correspondence: a.kasprawicz@we.umg.edu.pl (A.B.K.); ryszard.strzelecki@pg.edu.pl (R.S.)

**Abstract:** The article presents an induction generator connected to the power grid using the AC/DC/AC converter and LCL coupling filter. Three-level inverters were used in the converter, both from the generator side and the power grid side. The algorithm realizing Pulse Width Modulation (PWM) in inverters has been simplified to the maximum. Control of the induction generator was based on the Direct Field-Oriented Control (DFOC) method. At the same time, voltage control has been used for this solution. The MPPT algorithm has been extended to include the variable pitch range of wind turbine blades. The active voltage balancing circuit has been used in the inverter DC voltage circuit. In the control system of the grid converter with an LCL filter, the number of measurements was limited to the measurement of power grid currents and voltages. Synchronization of control from the power grid side is ensured by the use of a PLL loop with the system of preliminary suppression of undesired harmonics.

**Keywords:** induction generator; Direct Field-Oriented Control (DFOC); three-level inverter; Sinusoidal Pulse Width Modulator (SPWM); Maximum Power Point Tracking (MPPT)



**Citation:** Kasprawicz, A.B.; Husev, O.; Strzelecki, R. Induction Generator with Direct Control and a Limited Number of Measurements on the Side of the Converter Connected to the Power Grid. *Energies* **2023**, *16*, 63. <https://doi.org/10.3390/en16010063>

Academic Editor: Armando Pires

Received: 10 October 2022

Revised: 1 December 2022

Accepted: 14 December 2022

Published: 21 December 2022



**Copyright:** © 2022 by the authors. Licensee MDPI, Basel, Switzerland. This article is an open access article distributed under the terms and conditions of the Creative Commons Attribution (CC BY) license (<https://creativecommons.org/licenses/by/4.0/>).

## 1. Introduction

In times of energy crisis, various renewable energy sources are an extremely welcome alternative to conventional energy sources. In particular, small wind, hydroelectric, biomass, and biogas power plants are becoming increasingly popular in distributed generation systems [1,2]. They are often based on squirrel cage induction machines [3,4]. It is a cheaper solution than synchronous generators with electromagnetic excitation or permanent magnets, which are preferred mainly in the high-power range [5]. In addition, the induction machine, which keeps improving all the time [6], is also more straightforward, easier to operate, and more reliable. This is particularly important in the case of more demanding operating conditions or less qualified operators, such as on agricultural/animal farms [7,8].

An interesting case of using a squirrel cage induction machine as a generator is the Self-Excited Induction Generator (SEIG) system. Although the principle of the SEIG has been known for several decades [9,10], research in this area continues all the time [11–14]. The SEIG, first of all, it does not require an external power supply to excite the magnetic field and operates independently. Therefore, given its low price and high reliability, it is an attractive alternative generation system for use in stand-alone/island (off-grid) power systems. Furthermore, the sometimes-occurring need to enable the switching of an induction machine from off-grid to on-grid mode can be implemented either through algorithmic [15] or hardware solutions using power electronic converters, depending on the configuration of the target power system.

In the simplest case, an induction machine operating as an on-grid generator can be connected directly to the grid [4,16]. The connection does not require synchronization with

the grid (this is an important issue), and the start-up of the generator is like that of an induction motor. However, producing and delivering electricity to the grid is possible in this case only above a certain wind speed. Furthermore, it is not possible to electrically control the active power. In addition, when the machine is directly connected to the power grid, there is a demand for reactive power. This, of course, degrades the quality of electricity near the generator installation. Therefore, to improve the quality of electric power, there is a need to compensate for reactive power. For this purpose, battery capacitors are commonly used and possibly thyristor static compensators [4,17,18]. However, these approaches cannot satisfy the required power quality standards associated with connecting new power sources to the grid [19,20].

Currently, various novel electronic systems are used to prevent the negative impact of on-grid energy sources on the power grid [21–25]. In particular, AC/DC and DC/AC converters eliminate problems associated with injecting reactive and distorted currents into the grid. Near-sinusoidal currents with very low harmonic distortion are achieved by adequately controlling transistors and using small T-type Inductive–Capacitive–Inductive (LCL) coupling filters. The use of transistor power converters on the generator and grid sides has simultaneously enabled full conversion of generated power [4,26–28]. It also allowed the control of the active power given to the power grid. At the same time, an essential feature of systems with AC/DC/AC converters has become the possibility of their autonomous operation for dedicated consumers. This can occur in the event of a power outage from the grid or after self-excitation of the generator without grid involvement [27]. However, autonomous operation, widely considered in a great many publications, including [4,9–18], is not the subject of this article and will not be discussed.

An additional functionality of using converters is also the ability to control the reactive power. This solution also extends the wind speed range for which the power plant is able to transmit energy to the grid. The scope extension applies to lower and higher wind speeds at which currently existing systems have to be disconnected. Additionally, because the system has full conversion of electrical energy, it was possible to implement the tracking of the maximum power generated by the generator in a wide range of wind speed.

There are many methods to track the maximum power [4,29–34]. However, the most common are three basic MPPT algorithms. The first of these is an algorithm based on the known dependence of the wind turbine power in function of the angular speed  $P_G(\omega_m)$  [27]. The second one is based on the optimal speed ratio of the  $\lambda_{opt}$  turbine, but it requires the measurement of wind speed [30–33]. The third one is the incremental algorithm, which, without knowing the turbine parameters, continuously searches for operating conditions with maximum power for a given wind speed [34].

In the literature on the subject, including the work cited above, the research results on induction generators are primarily presented in relation to single problems. However, in the present study, the main goal is to cover the application problems of the squirrel cage induction machine as a generator cooperating with the power grid in a multifaceted manner, particularly in application to small-scale wind power plants.

In the proposed solution, three-level inverters were used, allowing the connection of both machines and local medium-voltage grids of the lower range. A simple control algorithm was developed for these inverters which does not require arrays or trigonometric functions. The algorithm is also easily adaptable for a larger number of voltage levels. These features greatly simplify the hardware implementation of the controller. In parallel, using Cascaded Delayed Signal Cancellation (CDSC) in combination with PLL resulted in better filtering of the fundamental harmonic of the line voltage required for synchronization and prediction in the control system.

To achieve high-quality sinusoidal current generated to the grid, a lossless LCL filter (without damping resistors) is used at the output of the inverter. In these cases, additional feedback from the measured state variables of the filter is typically implemented. This requires additional sensors. The authors estimated voltage across capacitors and

output current as an alternative to measurements. This reduced the number of required measurements and indirectly improved reliability as well.

In addition to the previously indicated improvements, the current solution for high wind speeds implemented a limitation of generated power by changing the angle of the wind turbine blades while the maximal power is maintained. In addition, the control system on the generator side uses forward feedback, making it possible to mitigate and accelerate transient processes in the event of rapid changes in wind speed. However, the active autonomous voltage balancing system on the capacitors used in the DC circuit not only improved the operation of three-level inverters, but also allows simple connection to the TN grid system.

### 2. Model of Wind Turbine

The induction generators in wind power plants are driven by wind turbines with different rotation axis arrangements. The case modeled in this article refers to the turbine with a horizontal axis of rotation. For this turbine, the mechanical power is given by (1).

$$P_m = 0.5\rho AV_w^3 C_p(\lambda, \beta) = 0.5\rho\pi R_b^2 V_w^3 C_p(\lambda, \beta) \tag{1}$$

where:  $C_p(\lambda, \beta)$  is the wind turbine power coefficient,  $V_w$  is the wind speed, and  $\rho$  is the air density (assumed  $\rho = 1.225 \text{ kg/m}^3$ ).

The power coefficient  $C_p(\lambda, \beta)$  in (1) is given by the empirical relation (2) [30].

$$C_p(\lambda, \beta) = 0.5176(116\lambda_i - 0.4\beta - 5)e^{-21\lambda_i} + 0.0068\lambda \tag{2}$$

$$\text{where : } \lambda_i = \frac{1}{\lambda + 0.08\beta} - \frac{0.035}{1 + \beta^3} \quad \lambda = \frac{\omega_T R_b}{V_w}$$

where:  $\lambda$  is the turbine blade tip speed ratio,  $\beta$  is the turbine blade setting angle,  $\omega_T$  is the angular speed of the turbine, and  $R_b$  is the turbine rotor radius.

In the simulation system, the wind turbine model described above was used to drive an induction generator. For the purposes of simulation tests, the dimensions of turbine blades  $R_b = 3 \text{ m}$  and gearbox  $G = 5$  were arbitrarily adopted (small wind power plant). The maximal power factor for the adopted model (2) was  $C_p(\lambda, \beta) = 0,48$  for  $\lambda = 8.1$ . The determined values refer to the zero setting angle of the turbine blades  $\beta = 0$ . Figure 1 shows the turbine power coefficient  $C_p(\lambda, \beta)$  for five different turbine blade pitch settings.

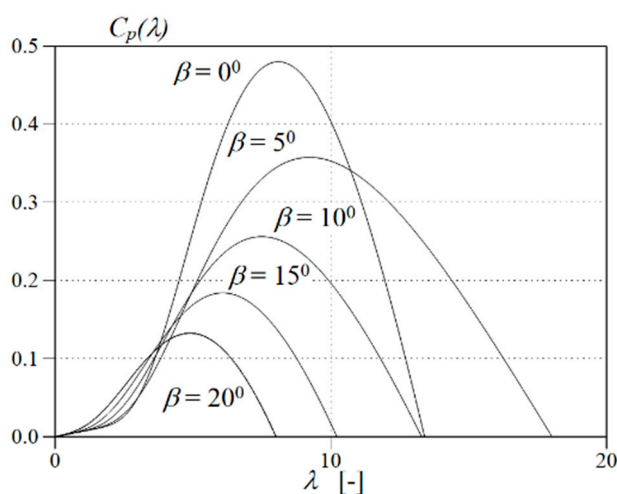


**Figure 1.** Power coefficient  $C_p(\lambda, \beta)$  as a function of the turbine speed ratio for five values of the setting angle.

However, Figure 2 shows the power of the turbine described above as a function of the angular velocity of the induction generator for different wind speeds with zero blade

angle adjustment. The diagram of maximum power is shown on the background of these characteristics. This waveform is described in Equation (3).

$$P_{\max} = c_{\beta} K (\omega_G / G)^3 \quad (3a)$$

$$c_{\beta} = \left( \frac{\lambda_{opt0}}{\lambda_{opt\beta}} \right)^3 \frac{C_p(\lambda_{opt\beta}, \beta)}{C_p(\lambda_{opt0}, 0^0)} \quad \text{where } K = 0.4223 \quad (3b)$$

Equation (3a) for  $c_{\beta} = 1$  describes the generator's maximum power  $P_{Gmax}$  for zero adjustment of the blade angle,  $\beta = 0$ . When the value of power generated exceeds the power rating of the generator  $P_N$ , the setting of the angle of the blades changes. To ensure the operation of the generator with the maximum power coefficient  $C_p(\lambda, \beta)$  under the new conditions, the coefficient  $c_{\beta}$  is also changed in accordance with the relation (3b).

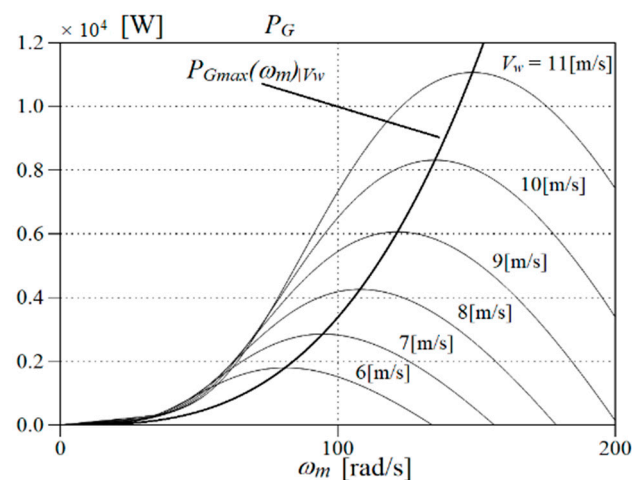


**Figure 2.** Generator power  $P_G$  in relation to the angular speed  $\omega_m$  for different wind speeds  $V_w$  and  $\beta = 0^\circ$ .

Equation (3a) is the basis for the implementation of the maximum power point tracking method. The tracking method based on the above equation will be used in the further part of the article in simulations of the wind farm system with an induction generator.

### 3. Multilevel Inverters Connecting the Generator to the Power Grid

At present, AC/DC/AC converters are commonly used in systems with full energy conversion [26,27]. Until recently, they were implemented on the basis of two-level inverters. However, multilevel inverters are increasingly being used [35,36]. An increased number of levels allowed them for better shaping of output currents at the same average number of joints of elements.

In the connection system of the induction generator to the power grid, three-level inverters were used from both the generator and the power grid side [33]. The types of inverters which were taken into consideration included: Neutral Point Clamped (NPC) inverter, and Neutral Point Piloted (NPP) inverter. Although the NPC inverters contain more elements, they have been accepted for further simulation studies. In the DC circuit, active balancing of voltage unbalance [37] was applied.

The scheme of a three-level inverter used in simulations on the generator and power grid side, with the active voltage balancing system, is shown in Figure 3.

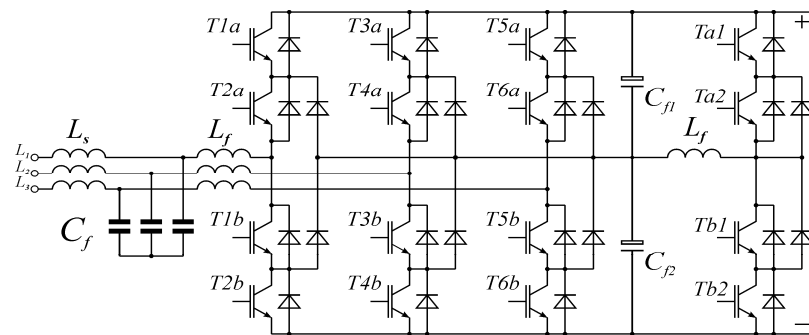


**Figure 3.** A three-level NPC inverter with autonomic voltage balancing on capacitors  $C_{f1}$  and  $C_{f2}$ .

#### 4. SPWM Modulator of Multilevel Inverter

A simple algorithm based on Sinusoidal Pulse Width Modulation (SPWM) has been used to generate control signals for a multilevel inverter. It is implemented independently for each phase.

At the initial stage, the set signals of phase voltages are modified by adding to them a waveform (4) that allows increasing the output voltage of the inverter.

$$\begin{cases} u_{kom} = \frac{\max(u_{aref}, u_{bref}, u_{cref}) + \min(u_{aref}, u_{bref}, u_{cref})}{2} \\ u_{xref} = u_{xref} - u_{kom} \quad x = a, b, c \end{cases} \quad (4)$$

The obtained modified signals are compressed to a range of  $\pm 2$  using the  $U_{DC}$  intermediate circuit voltage (5).

$$u_x = 2 \frac{u_{xref}}{U_{DC}} \quad x = a, b, c \quad (5)$$

In the next processing step, the signals were shifted by adding a constant component to them with a value of 2. As a result of this operation, unipolar signals in the range of values from 0 to 4 (6) were obtained.

$$u_{px} = u_x + 2 \quad x = a, b, c \quad (6)$$

Signals processed this way are analyzed in two ranges, in the range of values 0–2 and 2–4. In each of these intervals, the SPWM is implemented independently. In the range of values from 2–4, signals are generated for the upper transistors of each inverter branch  $T1a$ ,  $T3a$ ,  $T5a$  and in the range of values from 0–2 for the lower transistors  $T2a$ ,  $T4a$ ,  $T6a$ . The other inverter transistors are controlled by complementary signals  $T1b$ ,  $T3b$ ,  $T5b$  and  $T2a$ ,  $T4a$ ,  $T6a$  according to Figure 3.

The durations of the control signals for a single switching cycle of the transistors are calculated twice in advance of the half cycle after the prediction has been applied to the set signals. They are performed at the beginning and in the middle of the switching cycle. The control signals obtained in this way may be asymmetrical with respect to the center of the switching cycle. The implementation of the control described above, however, halves the delay in the system response to changes in the set point and load in relation to the single calculation of the signal duration only at the beginning of the switching cycle.

Simple mathematical relations, without trigonometric functions, significantly reduced the calculation time. In the initial phase, the implementation of the algorithm was limited to determining the range of the offset value of the set signal. The calculation procedure is started only after the preparation phase. In the case when the value of the set point signal is in the second range, the initial offset value should be subtracted before making the calculation. This operation is not required when the signal value is in the first range (7).

$$u_{rx} = \begin{cases} u_{px} - 2 & 2 < u_{px} < 4 \\ u_{px} & 0 < u_{px} < 2 \end{cases} \quad x = a, b, c \quad (7)$$

Eventually, the calculation of the delay times of the switching signals of the transistors, in relation to the beginning and the middle of the switching cycle, are performed based on dependencies (8).

$$T_a = (1 - 0.5u_{rx})T_p \quad x = a, b, c \quad (8)$$

where:  $T_p$  is half of the interval  $T_{pWMM}$ , and  $u_{rx}$  is the reduced value of the set voltage.

The switching delay time determined on the basis of the above dependence applies only to one transistor from the complementary pair in the phase. At that time, the transistor from the second complementary pair can be switched on for the time equal to half of the connection cycle (second interval) or off for the time equal to half of the connection cycle (first interval) (9). It depends on the actual value of the set signal.

$$\begin{bmatrix} T_{xi} \\ T_{x(i+1)} \end{bmatrix} = \begin{cases} (1 - 0.5u_{rx})T_p & 2 < u_{px} < 4 \\ 0 & 2 < u_{px} < 4 \\ T_p & 0 < u_{px} < 2 \\ (1 - 0.5u_{rx})T_p & \end{cases} \quad (9)$$

where:  $[x,i] \in \langle a,1;b,3;c,5 \rangle$ .

Figure 4 shows the waveforms of transistor control signals realized using the presented algorithm. They present the determined operating state of the three-level inverter.

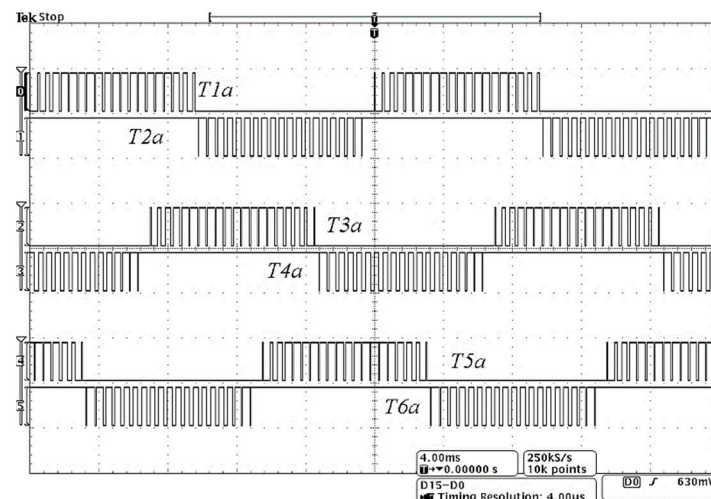


Figure 4. Control signals based on the proposed algorithm (experiment).

The above algorithm can be easily adapted for controlling the operation of inverters with a larger number of levels.

## 5. Field-Oriented Generator Control with Direct Orientation of the Vector (DFOC)

In the power plant system, the generator is a squirrel cage induction machine with the rated data in Appendix A.

Direct coupling of such a generator with the power grid is possible, but only in a very narrow range of angular velocities. In order to extend the speed range for which the generator will be able to supply energy to the power grid, a solution with full conversion based on the AC/DC/AC system was used. It forced the necessity of also using the converter on the generator side. In order to unify control systems and create the possibility of using medium-voltage generators in the future, three-level inverters were used.

The generator-side inverter control algorithm was based on field-oriented control with indirect field vector orientation with voltage control. It is relatively simple and allows setting the electromagnetic moment of the generator load. This is the starting point for the implementation of the MPPT algorithm. The cage induction motor model in the



of the rotor flux  $\psi_r^*$  and the motor torque  $m_e^*$ , the set currents  $i_{fd}^*$  and  $i_{fq}^*$  in the d–q axes are determined by means of PI type controllers in Equation (13). Next, on the basis of the set values of currents  $i_{fd}^*$  and  $i_{fq}^*$ , the set values of the output voltages  $u_{fd}^*$  and  $u_{fq}^*$  of the converter are also determined by means of PI type regulators in Equation (14).

$$\begin{cases} u_{fd}^*[k] = K_{P_{i_{fd}}} \left[ \left( i_{fd}^*[k] - i_{fd}[k] \right) \right. \\ \quad \left. + K_{I_{i_{fd}}} \sum_{m=0}^k \left[ \left( i_{fd}^*[m] - i_{fd}[m] \right) \right] \right] \\ u_{fq}^*[k] = K_{P_{i_{fq}}} \left[ \left( i_{fq}^*[k] - i_{fq}[k] \right) \right. \\ \quad \left. + K_{I_{i_{fq}}} \sum_{m=0}^k \left[ \left( i_{fq}^*[m] - i_{fq}[m] \right) \right] \right] \end{cases} \quad (14)$$

## 6. Predictive Control of the Power Grid Converter

The AC/DC/AC system's output converter works with the power grid directly. Its basic task is to supply energy generated by the generator to the grid. Thanks to the extended control algorithm, it can also act as a reactive power compensator.

In general, the grid voltage can be strongly distorted and contain higher harmonics with significant amplitudes. In the simulation tests, two harmonics were taken into account: 5 h with a value of 5% of the fundamental value of the harmonic and phase of  $30^\circ$  and 7 h with a value of 3% of the fundamental value of the harmonic and phase of  $-20^\circ$ . The condition of proper cooperation with the power grid is a good synchronization of the control system with the basic voltage harmonic. This goal was achieved using the PLL algorithm. However, when the network voltage is distorted, good synchronization is not sufficient to obtain the nearly sinusoidal voltage waveform with small content of higher harmonics. In order to perform the above task, the LCL filter was used in the inverter coupling system with the power grid, and the prediction in the control algorithm was applied [28,38–44]. The use of the filter in conjunction with the prediction has improved the shape of the grid current by reducing the content of higher harmonics below 1%.

The equivalent filter scheme is shown in Figure 6. It has a high damping factor of 60 dB/dec for frequencies above the resonant frequency. By appropriate selection of the resonant frequency, the modulation signal can be very effectively suppressed. However, it is a third-order filter and oscillations may occur in the output current, which must also be effectively suppressed.

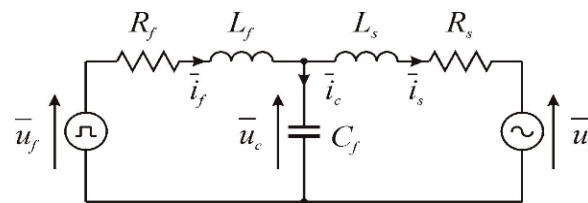


Figure 6. Equivalent LCL coupling filter scheme.

Equation (15a–c) describe the LCL filter in a continuous form.

$$\begin{cases} a) L_s \frac{d\vec{i}_s}{dt} + \vec{i}_s R_s = \vec{u}_c - \vec{u}_s \\ b) L_f \frac{d\vec{i}_f}{dt} + \vec{i}_f R_f = \vec{u}_f - \vec{u}_c \\ c) C_f \frac{d\vec{u}_c}{dt} = \vec{i}_f - \vec{i}_s \end{cases} \quad (15)$$



When switching to a discrete form, a description based on averaged momentary values of the grid voltage, inverter, and capacitor was used. Finally, the predictive control algorithm with the model was described using four-vector Equation (16).

$$\left\{ \begin{array}{l} \vec{u}_f[k+1|k+2] = \vec{u}_c[k+1|k+2] \\ \quad + (\vec{i}_f[k+2] - A_f * \vec{i}_f[k+1])/B_f \\ \vec{i}_f[k+2] = \vec{i}_s[k+2] + (\vec{u}_c[k+2|k+3] \\ \quad - A_f * \vec{u}_c[k+1|k+2])/B_f \\ \vec{u}_c[k+2|k+3] = \vec{u}_s[k+2|k+3] \\ \quad + (\vec{i}_s[k+3] - A_s * \vec{i}_s[k+2])/B_s \\ \vec{u}_c[k+1|k+2] = A_c * \vec{u}_c[k|k+1] \\ \quad + B_c * (\vec{i}_f[k+1] - \vec{i}_s[k+1]) \end{array} \right. \quad (16)$$

where:  $x[k+1|k+2]$  is average value of the quantity in the time interval  $k+1$  to  $k+2$ ,  $x[k+1]$  is value of the quantity at time  $k+1$ .

For a third-order filter, the prediction of two advance steps is required. In order to implement the control in the above equations, the grid current values were replaced with their set values:  $\vec{i}_s[k+2] = \vec{i}_s^*[k+2]$  and  $\vec{i}_s[k+3] = \vec{i}_s^*[k+3]$ . The remaining values were determined based on Equation (17).

$$\left\{ \begin{array}{l} \vec{u}_c[k-1|k] = \vec{u}_s[k-1] + (\vec{i}_s[k] - A_s * \vec{i}_s[k-1])/B_s \\ \vec{u}_c[k|k+1] = A_c * \vec{u}_c[k-1|k] + B_c * (\vec{i}_f[k] - \vec{i}_s[k]) \\ \vec{i}_s[k+1] = A_s * \vec{i}_s[k] + B_s * (\vec{u}_c[k|k+1] - \vec{u}_s[k|k+1]) \\ \vec{i}_f[k+1] = A_f * \vec{i}_f[k] + B_f * (\vec{u}_f[k|k+1] - \vec{u}_c[k|k+1]) \end{array} \right. \quad (17)$$

In the grid converter control system, the voltages on the capacitors and the converter output currents are not measured. However, these values are calculated. The average voltages  $\vec{u}_c[k-1|k]$  on the capacitors for the previous sampling period are estimated on the basis of the average values of the power grid voltage and the grid current in the previous sampling period. Then, based on the prediction, its values for the present moment are determined. In contrast, the converter output currents are calculated based on the prediction in the previous sampling period. The coefficients occurring in Equation (17) were determined based on the equations of the filter state and, assuming the constancy of the element parameters, they can be calculated based on the dependence (18).

$$\left\{ \begin{array}{ll} A_s = 1 - \exp(-T_s/T_e) & B_s = (1 - A_s)/R_s \\ A_f = 1 - \exp(-T_s/T_f) & B_f = (1 - A_f)/R_f \\ A_c = 1 - \exp(-T_s/T_c) & B_c = (1 - A_c) * R_c \\ T_e = L_s/R_s & T_f = L_f/R_f \quad T_c = C_f R_c \end{array} \right. \quad (18)$$

In Equations (16) and (17), the average grid voltage was used for the intervals  $[k|k+1]$ ,  $[k+1|k+2]$ , and  $[k+2|k+3]$  and the currents from the moment of measurement  $[k]$ . The averaging refers to half of the switching cycle of transistors. The coefficients in the equations include such parameters of the coupling system as the filter inductances  $L_s$  and  $L_f$ , filter resistances  $R_s$  and  $R_f$ , as well as capacitance  $C_f$  and resistance  $R_c = \text{ESR}$ .

The voltage values of the power grid at the time  $[k+1]$ ,  $[k+2]$ , and  $[k+3]$  were determined by summing (21) rotated vectors, basic (19) and higher harmonics (20), and grid voltage. On the other hand, the size of the rotation angle of the vector components depends on their pulsation  $\omega_{P11h}$ ,  $\omega_{mh}$ , and sampling time  $T_s$ .

$$\vec{u}_{sP11h}[k+n] = \vec{u}_{sP11h}[k](\cos(nd\gamma_{P11h}) + j \sin(nd\gamma_{P11h}))$$

where :  $d\gamma_{P11h} = 2PIf_{P11h}T_s \quad n = 1, 2, 3$  (19)

$$\vec{u}_{smh}[k+n] = \vec{u}_{smh}[k](\cos(nd\gamma_{mh}) + j \sin(nd\gamma_{mh}))$$

where :  $d\gamma_{mh} = 2PIf_{mh}T_s \quad m = 5, 7, \dots \quad n = 1, 2, 3$  (20)

$$\vec{u}_s[k+n] = \vec{u}_{sP11h}[k+n] + \sum_m \vec{u}_{smh}[k+n]$$

where :  $n = 1, 2, 3 \quad m = 5, 7, \dots$  (21)

The components of the current  $i_{s\alpha\beta}$  and  $i_{f\alpha\beta}$  for time  $[k+1]$  (17) are determined based on prediction with the model of coupling circuit, Figure 6.

The set value of the current was determined based on the definition of instantaneous powers for the first harmonic, given by Hirofumi Akagi (22) [45,46].

$$\begin{cases} p^*[k] = u_{s\alpha P11h}[k]i_{s\alpha}^*[k] + u_{s\beta P11h}[k]i_{s\beta}^*[k] \\ q^*[k] = u_{s\beta P11h}[k]i_{s\alpha}^*[k] - u_{s\alpha P11h}[k]i_{s\beta}^*[k] \end{cases}$$
 (22)

It refers to the actual time  $[k]$ . However, in relations (16), values of currents are also required for times  $[k+2]$  and  $[k+3]$ . Assuming that the power grid current should have the sinusoidal waveform, the required quantities can be easily obtained. For this purpose, the rotation of the reference current vector is carried out twice and three times, determined for the instant  $[k]$  based on the dependence (22), by the angle determined from the fundamental harmonic voltage of the power grid frequency  $f_{P11h}$  of network voltage and the sampling interval  $T_s$  (23).

$$\vec{i}_s^*[k+n] = \vec{i}_s^*[k](\cos(n * d\gamma_{P11h}) + j \sin(n * d\gamma_{P11h}))$$

where :  $d\gamma_{P11h} = 2PIf_{P11h}T_s \quad n = 2, 3$  (23)

Figure 7 shows a block diagram of the grid converter control algorithm based on the presented dependencies.

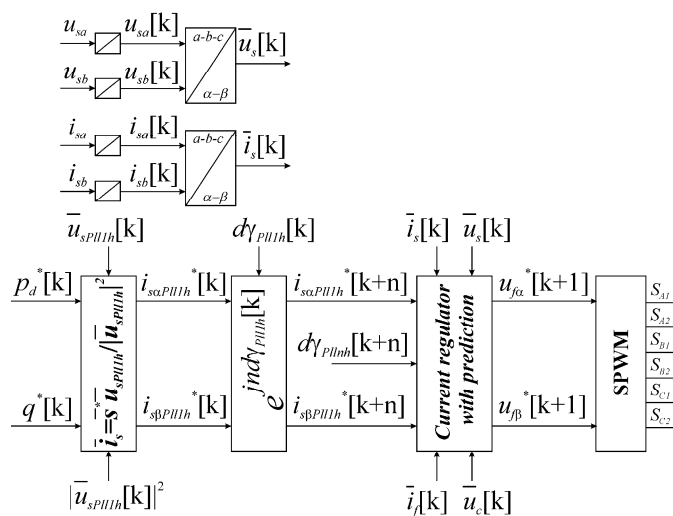


Figure 7. Block diagram of the grid converter control algorithm.

### 7. Synchronization of Control to the Voltage of the Power Grid

As mentioned earlier, the control of the converter, which is connected to the power grid, requires precise synchronization with the voltage waveform. In the presented system, this process takes place in two stages. In the first stage, thirty-two positive-order and thirty-two negative-order higher harmonics are attenuated using a cascaded system  $CDSC(v_{\alpha\beta})_{2,4,8,16,32,64}$  [47–52]. A valuable feature of this system is that it does not introduce, or introduces a negligibly small value of, phase shift of the input waveform first harmonic.

The second stage is proper synchronization with the fundamental harmonic of the power grid voltage. Figure 8 shows the implemented synchronization system.

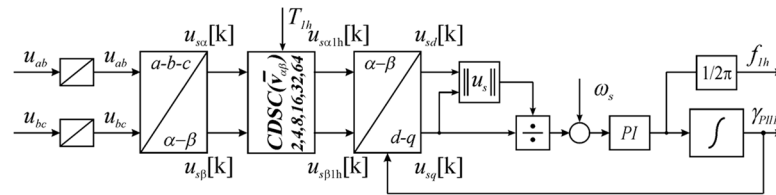


Figure 8. Block diagram of CDSC–PLL system.

### 8. Wind Power Plant System

Figure 9 shows a complete block diagram of a wind power plant connected to the power grid by three-level inverters. The connection between the power plant and the power grid is constituted by an LCL filter with the parameters given in Appendix B. In the DC circuit, there is a voltage balancing system on capacitors  $C_{f1}$  and  $C_{f2}$ . Between the control systems, generator, and power grid inverter, feed-forward power feedback has been used. It speeds up the transient processes in the converter system at wind changes.

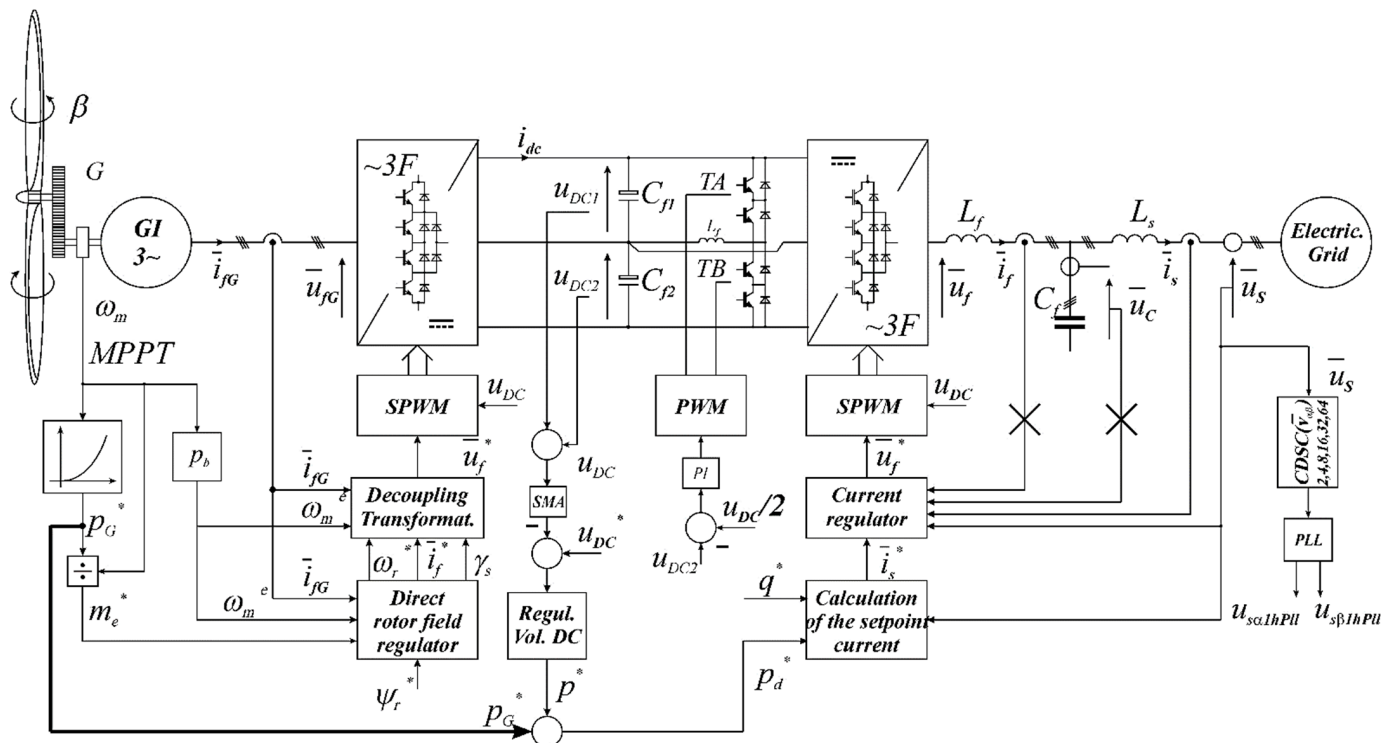


Figure 9. Wind power plant with an induction generator and AC/DC/AC converter based on three-level inverters.

### 9. Laboratory Tests of a Wind Power Plant

The tests of the system were carried out by simulation using the software package PLECS version 4.4.3, and the limited physical experiment. From this package, only library

elements of the main circuit were used for modeling. These elements include: model of induction motor, transistors, inductances, and capacitances, as well as current, voltage, and speed measurement systems. The control algorithm was written in the C programming language. After compiling, in the form of a dynamic library \*.dll, it was attached to the main program modeling system. The control algorithm is called from the main program every 50 μs (20 kHz) similarly as in the real system as part of the interrupt service. However, the frequency of switching of transistor keys is halved and in the tested system it is 10 kHz.

The procedure presented above was dictated by the fact that in the case of experimental implementation, the tested algorithm can be easily transferred to a microprocessor controller with minor modifications to adapt it to the hardware equipment. The laboratory research process carried out in this way will reproduce the working conditions of the real system fairly reliably.

During the simulation tests, the wind was modeled changing in the cycle from 6 m/s to 9 m/s and further to 11 m/s and from 11 m/s to 9 m/s, finishing at 6 m/s with phases of constant speed value. The operation of the system for the above test scenario is given in Figure 10, which shows the assumed changes in wind speed  $V_w$  and the corresponding changes in angular speed  $\omega_G$  and power  $P_G$  of the generator, as well as in power  $P_S$  supplied to the power grid.

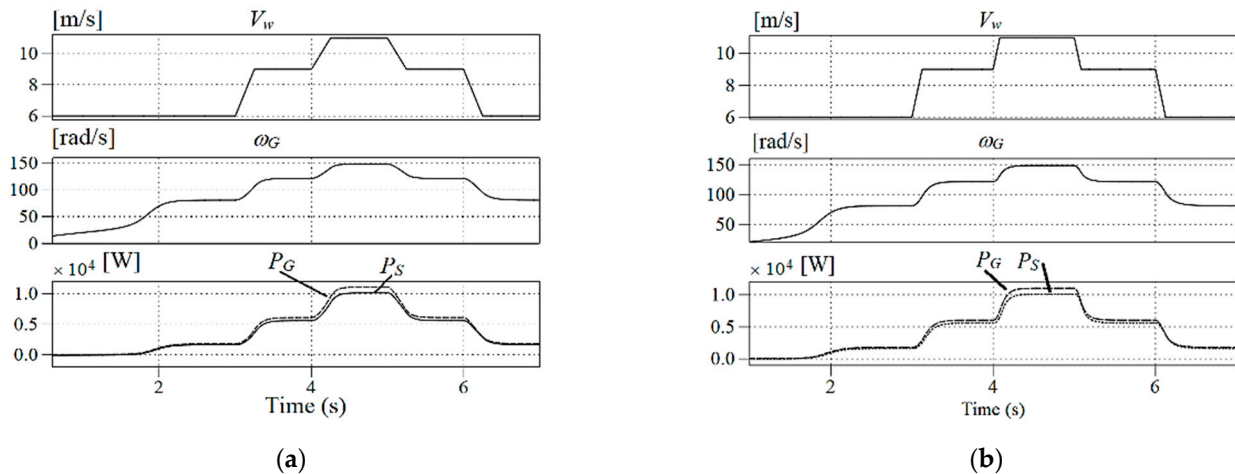


**Figure 10.** Assumed changes in wind speed  $V_w$  (a) 12, 8, -8, -12 [m/s<sup>2</sup>]; (b) 24, 24, -24 -24 [m/s<sup>2</sup>] and corresponding changes in angular velocity  $\omega_G$ , generator power  $P_G$ , and power grid  $P_S$ .

Figure 11a shows the waveforms of generator power  $P_G$  as a function of its angular speed  $\omega_G$ , while Figure 11b presents the waveform of wind turbine power coefficient  $C_p(\lambda, \beta)$ . These two waveforms were obtained for different wind speeds at a constant turbine blade pitch  $\beta = 0^\circ$ . Power values at which changes start, after changes in wind speed, allow conclusions on the good implementation of the maximum power point tracking in steady states.

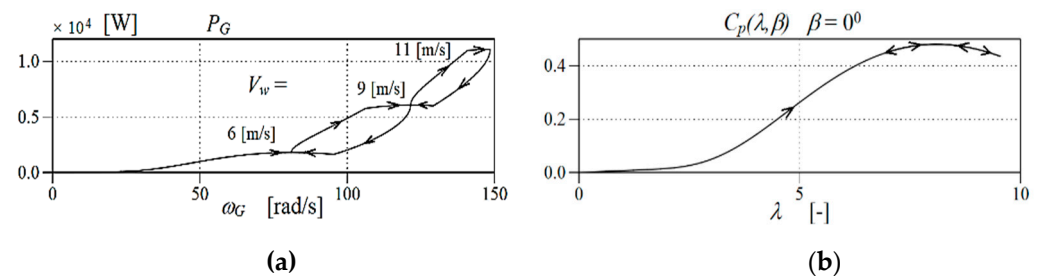


**Figure 11.** Waveforms of generator power  $P_G$  (a) and turbine power coefficient  $C_p(\lambda, \beta)$  (b) for changing wind speed  $V_w$  and blade angle equal to  $\beta = 0^\circ$ .

Figures 12 and 13 show changes in wind speed  $V_w$ , angular speed  $\omega_G$ , and power of generator  $P_G$  as well as of power  $P_S$  supplied to the power grid. The presented waveforms refer to the case of a wind speed increase from 9 m/s through 12 m/s up to 14 m/s, and a decrease within the same range. When the wind speed exceeded 11 m/s, the generated power was higher than the rated power of the generator. In order to limit the power, the angle of the wind turbine blades' setting was changed from  $\beta = 0^\circ$  to  $\beta = 10^\circ$  to reduce the generated power. Despite this change, the wind power plant continues to work with the tracking of the maximum power point by correcting the coefficient  $c_\beta$  in accordance with Equation (3b). On the basis of the waveform, Figure 10 shows the efficiency of the system, which, for a predetermined wind velocity  $V_w = 11$  m/s and an angle  $\beta = 0^\circ$ , was  $\eta \cong 91.2\%$ .

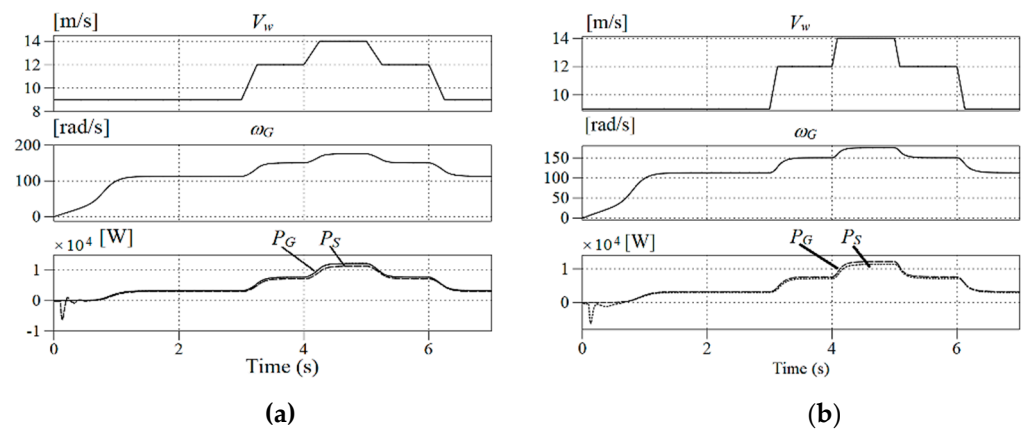


Figure 12. Waveforms of wind speed  $V_w$  (a) 12, 8, -8, -12 [m/s<sup>2</sup>]; (b) 24, 24, -24 -24 [m/s<sup>2</sup>] generator angular speed  $\omega_G$  and power  $P_G$ , and grid power  $P_S$ , for  $\beta = 10^\circ$ .

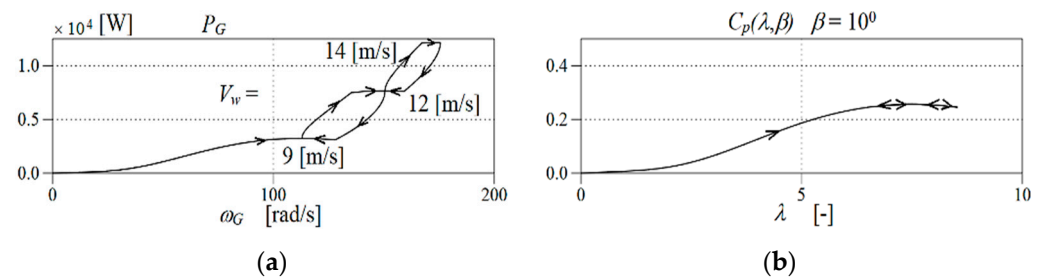
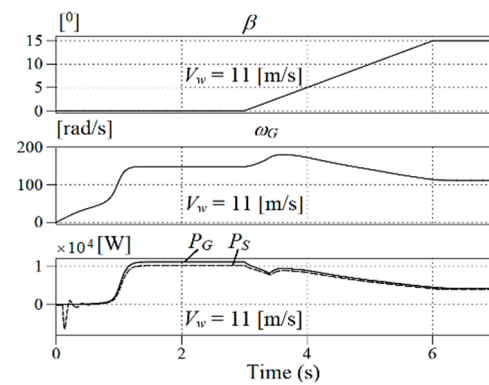


Figure 13. Waveforms of generator power  $P_G$  (a) and turbine power coefficient  $C_p(\lambda, \beta)$  (b) for changing wind speed  $V_w$  and blade angle equal to  $\beta = 10^\circ$ .

Figures 14 and 15 show the transient processes occurring in a wind power plant during a linear change in the turbine blade angle setting in the range from  $\beta = 0^\circ$  to  $\beta = 15^\circ$ , at constant wind speed. In the initial phase of changes in  $\beta$ , a slight increase in generator angular speed  $\omega_G$  is observed, but then it decreases to the final steady-state level below the initial speed. As a result, the power factor  $C_p(\lambda, \beta)$  decreases (Figure 15b) from the optimal value for the set wind speed  $V_w = 11$  m/s and angle  $\beta = 0^\circ$  to the optimal value for the angle  $\beta = 15^\circ$ . Therefore, the power  $P_G$  generated and  $P_S$  supplied to the power grid are also decreasing (Figures 14 and 15a).

Figure 16 shows voltage  $u_{abG}$  and current  $i_{aG}$  waveforms on the generator inverter side. The waveforms on the left refer to the change in wind speed in the range from 6 to 9 m/s, while on the right side the wind speed varies from 9 to 6 m/s. The center waveforms show the steady state of the generator at wind speed of 11 m/s. Despite the wide range of wind speed variations, the converter work is correct. The converter passes without disturbance to the three-level mode when the wind speed increases and vice versa to the two-level mode while reducing the wind speed. The obtained waveforms indicate the correct operation of the system in various conditions.



**Figure 14.** The waveforms of the angle of the wind turbine blades  $\beta$ , the angular velocity  $\omega_G$ , the power  $P_G$  and supplied to the power grid  $P_S$ .

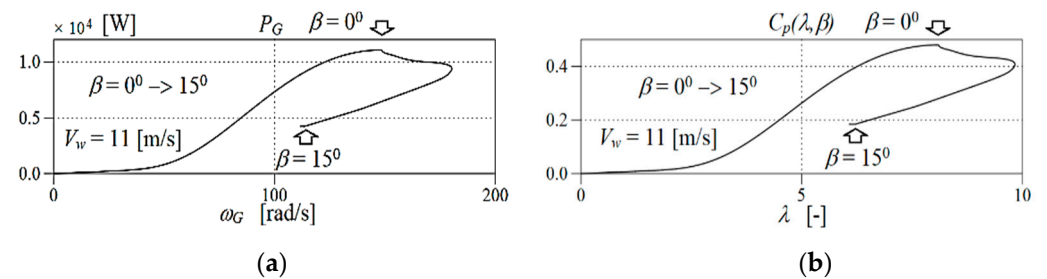


**Figure 15.** Waveforms of generator power  $P_G$  (a) and turbine power coefficient  $C_p(\lambda, \beta)$  (b) for constant wind speed and blade setting angle  $\beta$  changing from  $0^\circ$  to  $15^\circ$ .

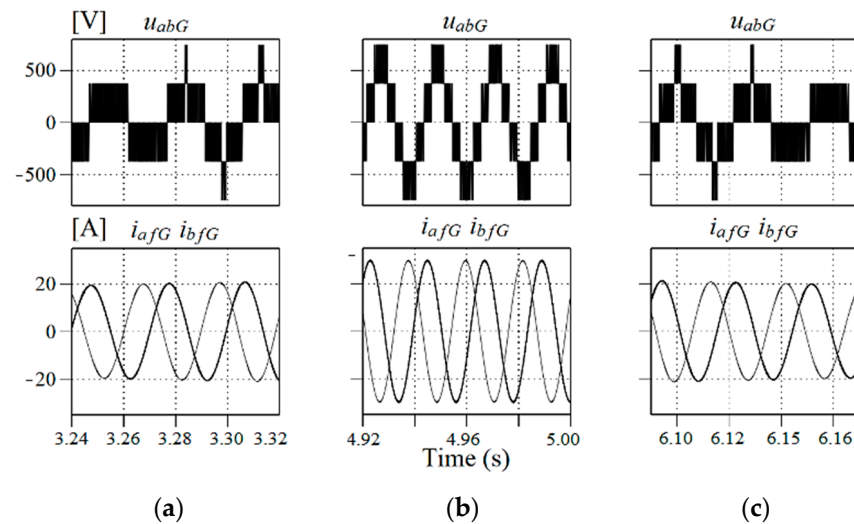


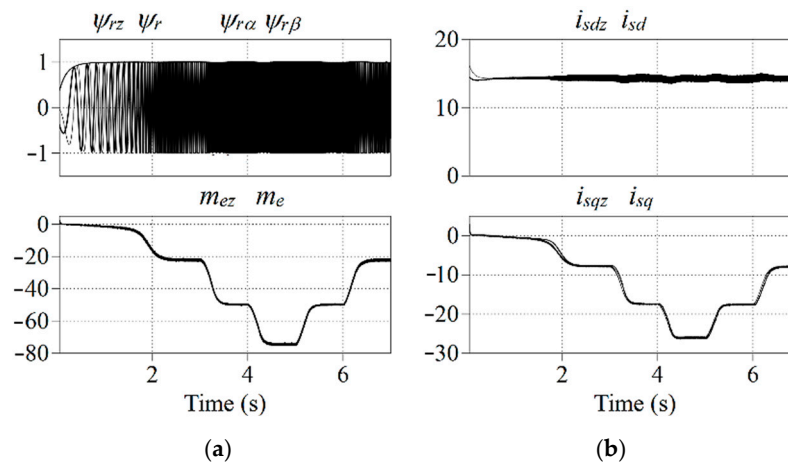
**Figure 16.** Waveforms of generator voltage  $u_{abG}$ , and currents  $i_{afG}$ ,  $i_{bfG}$  at changing (a), (c) and constant wind speed equal to 11 m/s (b).

The proposed simplified algorithm of the three-level inverter modulator works correctly. This is confirmed by the simulation results obtained. Switching processes of transistors are ordered and there is no uncontrolled switching in them as evidenced by voltage waveforms.

In all of the above cases, the generator current is close to sinusoidal with a low content of higher harmonics (Figure 16). Higher harmonics generate pulsating torque and increase the loss of the induction generator so they lack a positive effect on the system.

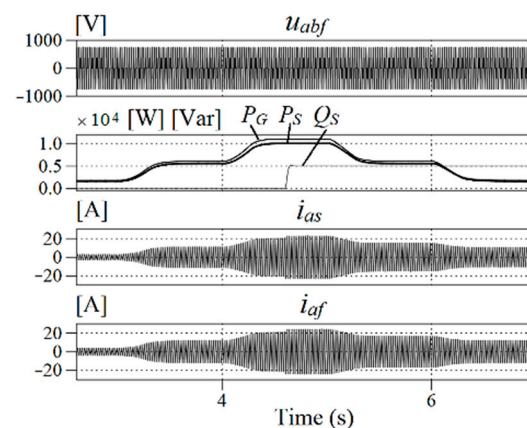
Figure 17a shows the setpoints and measured quantities in the direct control system for the rotor flux and electromagnetic torque of an induction generator. Figure 17b, on the

other hand, shows the corresponding setpoints and measured values of the stator current components in a coordinate system rotating synchronously with the rotor flux.



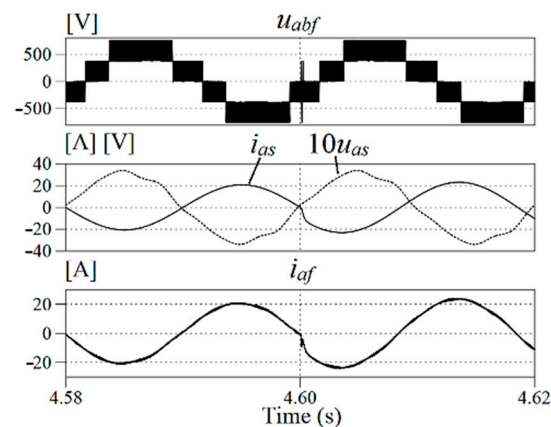
**Figure 17.** The waveforms of: (a) the set rotor flux  $\psi_{rz}$ , the set driving torque of a wind turbine  $m_{ez}$  and estimated values  $\psi_r$  and electromagnetic torque of generator  $m_e$ ; (b) the set current components in the d and q axes and their measured values.

Figure 18 shows the voltage waveforms  $u_{abf}$  of the converter connecting the system to the power grid, the power of the induction generator  $P_G$ , power supplied to the power grid  $P_S$ , and reactive power  $Q_S$ . In the lower part of the figure the waveforms of the power grid current  $i_{as}$  and the output current of the inverter  $i_{af}$  are shown. The waveforms were obtained during the sequence of wind speed changes from 6 m/s by 9 m/s to 11 m/s and in the opposite direction of changes ending with the wind speed of 6 m/s.



**Figure 18.** Waveforms of the generator's phase-to-phase voltage  $u_{abf}$ , power output  $P_G$ , power supplied to the grid  $P_S$ , reactive power  $Q_S$ , grid current  $i_{as}$ , and inverter current  $i_{af}$ .

In the waveforms, an increase in the current can be observed at the moment of setting reactive power. Figure 19 shows in detail the steady state of the power plant operation at a wind speed of 11 m/s with a load determined from the operation of the MPPT system. To fully illustrate the system's capabilities at time  $t = 4.6$  s, the reactive power of  $Q_S = 5$  kVar was applied to the grid converter control system (Figure 18). This caused temporary additional switching of the inverter transistors. They are clearly visible in the output waveform of the  $u_{abf}$  inverter (Figure 19). They cause immediate displacement of the  $i_{as}$  current grid phase (Figure 19). However, a fast change in the output current phase does not lead to oscillations. Thanks to the use of advanced control, it was possible to avoid unfavorable oscillation phenomena in the output current of the multilevel inverter.



**Figure 19.** Waveforms of the phase-to-phase voltage of the power grid inverter  $u_{abf}$ , voltage  $u_{as}$  and current  $i_{as}$  of the grid, and inverter current  $i_{af}$  for change in reactive power.

Despite the strong distortion of the power grid voltage, which includes 5 h with a value of 5% and 7 h with a value of 3% of the fundamental value of the harmonic, the current waveform  $i_{as}$  is close to sinusoidal with the content of higher harmonics below 1% (Table 1). The content of higher harmonics of the power grid current has not changed much with the changes in load and type of control (where:  $f_G$ —generator voltage frequency).

**Table 1.** The content of higher harmonics.

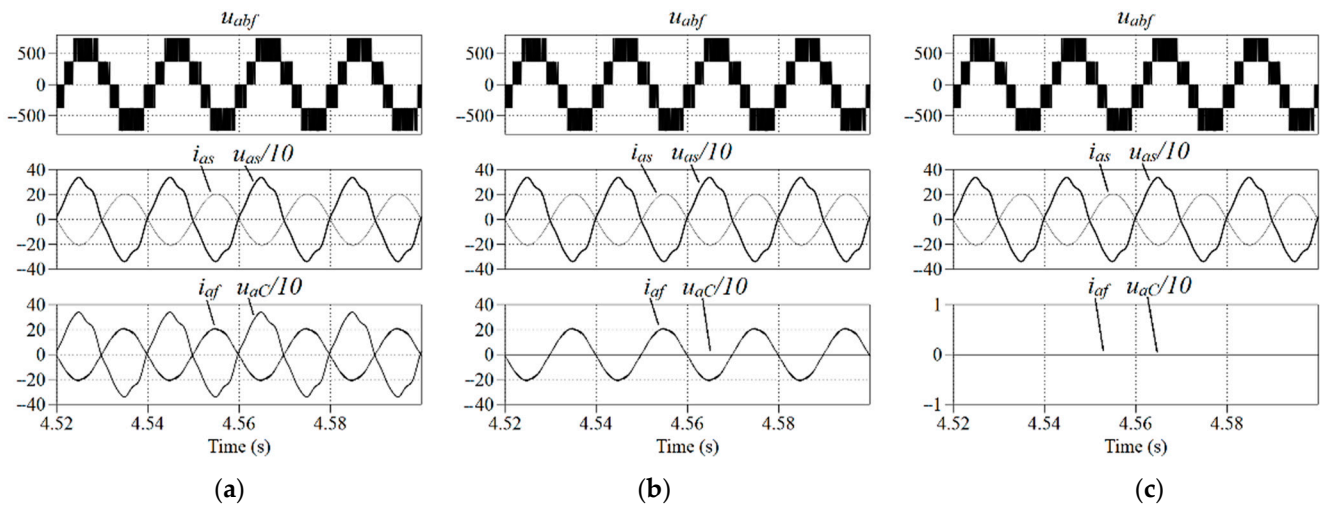
Type of System	$P_s$ [kW]	$f_G$ [Hz]	Content of Higher Harmonics			
			THD_IG%	THD_US%	THD_If%	THD_Is%
With all measurements	5.5	37.39	0.83	5.83	5.26	0.18
	10.0	45.40	0.61	5.76	2.68	0.05
Without measurement $u_c$	5.5	37.41	0.83	5.83	5.29	0.18
	10.0	45.40	0.61	5.83	2.68	0.05
Without measurement $u_c, i_f$	5.5	37.39	0.83	5.83	-	0.695
	10.0	45.40	0.61	5.83	-	0.37

In the presented waveforms, the correct operation of the proposed simplified modulators can be also observed in the case of a converter connected to the power grid (Figure 19). Lack of asymmetry of the output voltages of the three-level inverter proves the proper operation of the balancing voltage in the DC voltage circuit. Figure 20 shows the voltage and current waveforms after connecting the system to the power grid. In spite of the strongly deformed voltage waveform, the obtained current is close to sinusoidal.

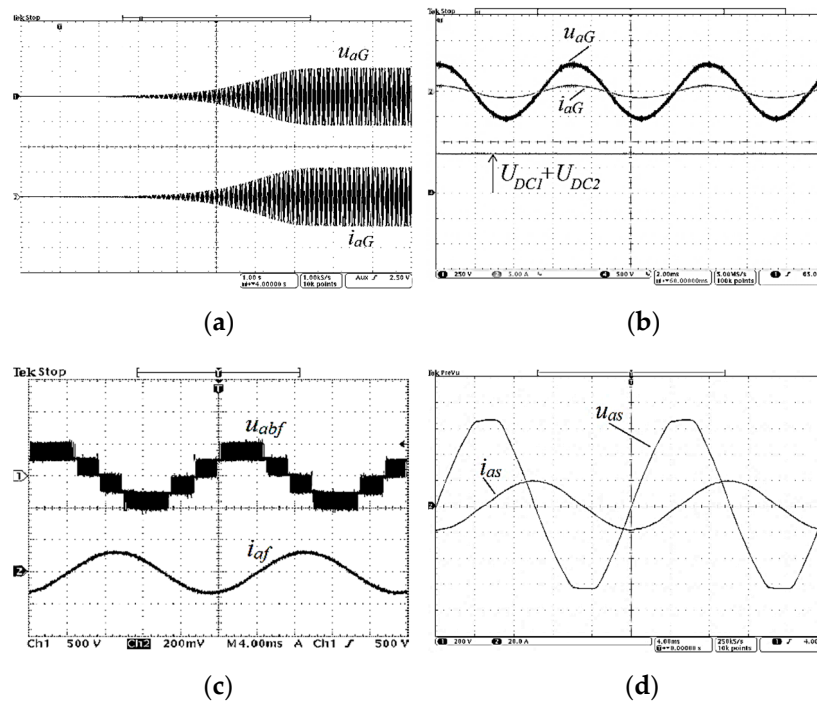
Based on the simulation tests performed, the correct operation of the small wind power plant system was observed. The power plant's control algorithm efficiently tracks the point of maximum power, both in the case of changes in wind speed and changes in the angle of setting the wind turbine blades.

Figure 21 shows an example of experimental results from testing an induction generator on the test stand shown in Figure 22. In particular, Figure 21a documents the sinusoidal waveform of the line current despite the high distortion of the grid voltage. These results confirm the efficiency of a simplified three-level inverter modulator without the use of arrays and trigonometric functions, as well as the immunity to voltage distortion in the real power supply network.





**Figure 20.** Voltage waveforms  $u_{abf}$  and current  $i_{af}$  of the inverter,  $u_{abs}$  voltage and current  $i_{as}$  of the power grid, and  $u_{ac}$  capacitor voltage in steady state (a) with all measurements, (b) without measuring the capacitor voltage, (c) without measuring the inverter current and capacitor voltage.



**Figure 21.** Selected experimental waveforms of voltage and current in the investigated generator system (Figure 9): (a) voltage and current of the induction machine during the start-up, (b) voltage and current of the induction generator, and DC link voltage at steady state, (c) output voltage and current of the grid inverter, (d) voltage and current of the power grid for reactive power.

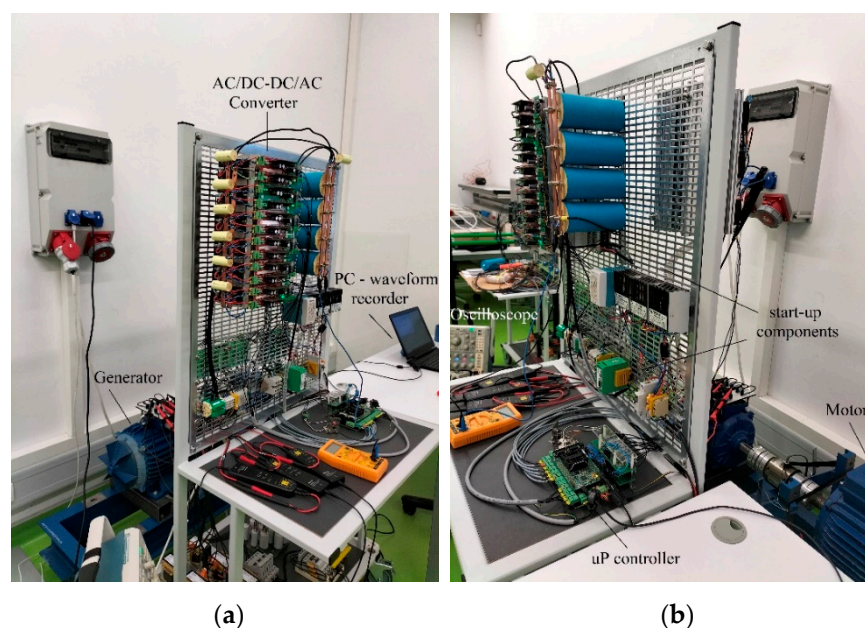


**Figure 22.** Experimental stand for testing of induction generator system (Figure 9): (a) left side view, (b) right side view.

## 10. Conclusions

The article presents a complete control algorithm for the AC/DC/AC converter connecting the induction generator with the power grid. The algorithm for controlling the DC/AC converter from the power grid does not use measurements of output currents or voltages on the LCL filter capacitors. These values are estimated on the basis of measurements of power grid currents, voltages, and filter parameters.

The application of the converter with the proposed control algorithm provided near-sinusoidal currents of the power grid. Thanks to the LCL filter coupling the system with the power grid and the predictive control, the content of higher harmonics in the output current below  $\sim 1\%$  was obtained, despite the assumption of high voltage distortion (Figures 19 and 20) and limiting the number of measurements of the input quantities. Correct operation of the system was also achieved with the proposed modulator for the multilevel inverter. The system also performs the function of a reactive power compensator thanks to the possibility of controlling the phase of the current in relation to the grid voltage.

However, to control the AC/DC converter from the induction generator side, the algorithm of direct rotor flux and torque control was used. The current distortion on the generator side is slightly higher (Figure 21a) and this is due to the lack of an additional coupling filter (Figure 9). This lack is partially compensated by the relatively high inductance of the induction motor. The low content of higher harmonics of the current does not significantly affect the pulsation of the generator's load torque and increasing losses.

Original simple algorithms of modulators do not require trigonometric functions or arrays for calculations. This reduced the time needed to calculate the switching times of inverter transistors. The use of full processing of the produced energy extends the use of an induction generator to a range of lower wind speeds.

The article proposes a modification of the maximum power point tracking method. It concerns the range of higher wind speeds, in which a change in the angle of the wind turbine blades' setting is required. The modification was implemented by introducing the correction factor  $c_\beta$  to the dependence (3). This enabled the use of an induction generator with a maximum power factor  $C_p$  for wind speeds varying within wide limits.

In the studies, the presented system was characterized by high efficiency, which for different loads and operating systems is shown in Table 2.

**Table 2.** Total efficiency of generator systems.

$P_s$ [kW]	With all Measurements	Without Measurement $u_c$	Without Measurement $u_c, i_f$
	$\eta$ %	$\eta$ %	$\eta$ %
1.6	91.02	91.02	91.07
5.5	92.74	92.74	92.67
10.0	91.77	91.77	91.75

The promising results of the system test encourage further work. The high complexity of the control algorithm presented in the article requires the use of a microprocessor controller with high computing power. Therefore, all the required computational procedures were also written in the “C” programming language with a minimal number of instructions. This guarantees relatively short control times in the real system.

The proposed system was characterized by fewer measurements than are required in typical systems. By using estimation and prediction, the number of measurement channels was reduced by four. At the same time, the system did not show oscillations or a significant increase in the content of higher harmonics in the power grid current. The efficiency of the system also did not noticeably deteriorate. At the same time, the reduced number of measurements increases reliability and reduces implementation costs. The applied control method does not require additional damping resistances in the LCL coupling circuit. At the stage of practical implementation of the control, the requirements for the selection of a microprocessor controller are also fully acceptable.

The squirrel cage induction machine (SEIG) used in the presented generation system is an efficient, less expensive, and fully functional alternative to PMSG in application to small-scale residential power plants. Currently, implementation work is underway to start production of the developed solution with a capacity of 10-50kW for widespread use in rural households.

**Author Contributions:** Conceptualization: R.S. and A.B.K.; Formal analysis: A.B.K.; Validation: A.B.K. and O.H.; Methodology: A.B.K. and O.H.; Investigation: A.B.K.; Writing—original draft: A.B.K. and R.S.; Writing—review and editing: R.S. and O.H.; Supervision: R.S. and O.H.; Project administration and Funding acquisition: R.S. All authors have read and agreed to the published version of the manuscript

**Funding:** The project is financed by the Program of the Ministry of Science and Higher Education “Regional Excellence Initiative” from the years 2019–2022, project number 006/RID/2018/19, grant amount PLN 11 870 000, realized at the Gdynia Maritime University, Poland.

**Conflicts of Interest:** The funders had no role in the design of the study; in the collection, analyses, or interpretation of data; in the writing of the manuscript, or in the decision to publish the results.

### Abbreviations

SEIG	Self-Excited Induction Generator
AC/DC	AC to DC converter
DC/AC	DC to AC converter
MPPT	Maximum Power Point Tracking
NPC	Neutral Point Clamped inverter
NPP	Neutral Point Piloted inverter
SPWM	Sinusoidal Pulse Width Modulation
PWM	Pulse Width Modulation
DFOC	Direct Field-Oriented Control
CDSC	Cascaded Delayed Signal Cancellation
PLL	Phase Locked Loops
THD <sub>I<sub>G</sub></sub>	Total Harmonic Distortion of the generator current
THD <sub>I<sub>S</sub></sub>	Total Harmonic Distortion of the power grid current

$THD_{I_f}$	Total Harmonic Distortion of the inverter current
$THD_{U_s}$	Total Harmonic Distortion of the power grid voltage
$PI$	Proportional–Integral controller
$ESR$	Equivalent Series Resistance
$GI$	Induction Generator
$SMA$	Smoothing Moving Average
<b>Symbols</b>	
$C(\lambda, \beta)$	wind turbine power coefficient
$\lambda$	speed factor
$\beta$	blade angle
$V_w$	wind speed
$\rho$	air density
$\omega_m$	angular velocity of the induction generator
$c_\beta$	reduced power factor
$A$	surface area swept by wind turbine blades
$R_b$	dimensions of turbine blades
$G$	gearbox
$P_{Gmax}$	maximum power of the generator
$u_{xref}$	phase reference voltages $x = a, b, c$
$u_{kom}$	common voltages
$U_{DC}$	DC link voltage
$u_x$	normalized phase control voltage $x = a, b, c$
$u_{px}$	unipolar phase control voltage $x = a, b, c$
$u_{rx}$	determination of the voltage ranges of the set phases $x = a, b, c$
$T_p$	period of PWM
$T_{xi}$	switching period of transistors of individual phases $[x, i] \in \langle a, 1; b, 3; c, 5 \rangle$
$T_r$	electrical constant of the rotor circuit
$L_r$	inductance of the motor rotor
$R_r$	resistance of the motor rotor
$L_m$	main inductance of the motor
$\omega_r$	slip pulsation
$\psi_r$	rotor flux vector
$i_{fG}$	generator current vector
$i_{fd}, i_{fq}$	components of the generator current vector in the d–q system
$p_b$	number of generator pole pairs
$m_e$	electromagnetic moment of the generator
$R_s, R_f$	filter inductance resistances
$L_s, L_f$	filter inductances
$C_f$	filter capacity
$R_c$	equivalent series resistance
$u_s, u_c, u_f$	voltage of the power grid, capacitor, grid inverter
$i_s, i_c, i_f$	currents of the power grid, capacitor, grid inverter
$T_e, T_f, T_c$	time constants of the filter
$T_s$	sampling time constant

### Appendix A. Induction Motor (Generator)

1. Type: BBC QV 160M4AA
2. Nominal parameters:

$P_N$ [kW]	$U_{IN}$ [V]	$I_{IN}$ [A]	$f_{IN}$ [Hz]	$n_N$ [rpm]	$2p$ [-]	$\cos\phi_N$
11	400	22.5	50	1438	4	0.83

3. Electrical parameters:

$R_s$ [ $\Omega$ ]	$L_{\sigma s}$ [mH]	$R_r$ [ $\Omega$ ]	$L_{\sigma r}$ [mH]	$L_m$ [mH]	$J$ [kgm <sup>2</sup> ]
0.3223	1.99	0.4762	3.4	69.69	0.194



## Appendix B. LCL Filter

Electrical parameters:

$R_f[\Omega]$	$L_f[\text{mH}]$	$R_s[\Omega]$	$L_s[\text{mH}]$	$C_f[\mu\text{F}]$
0.1	2.0	0.05	1.0	10.0

## References

- Gharehpetian, G.B.; Mousavi Agah, S.M. Distributed Generation Systems. In *Design, Operation and Grid Integration*; Elsevier: Amsterdam, The Netherlands, 2017.
- Buchholz, B.M.; Styczynski, Z.A. *Smart Grids: Fundamentals and Technologies in Electric Power Systems of the Future*; Springer: Berlin/Heidelberg, Germany, 2021.
- Mahela, O.P.; Gupta, N.; Khosravy, M.; Patel, N. Comprehensive Overview of Low Voltage Ride Through Methods of Grid Integrated Wind Generator. *IEEE Access* **2019**, *7*, 99299–99326. [\[CrossRef\]](#)
- Simões, M.G.; Farret, F.A. *Renewable Energy Systems: Design and Analysis with Induction Generators*; Power Electronics and Applications Series; CRC Press: Boca Raton, FL, USA, 2004.
- Yaramasu, V.; Wu, B.; Sen, P.C.; Kouro, S.; Narimani, M. High-power wind energy conversion systems: State-of-the-art and emerging technologies. *Proc. IEEE* **2015**, *103*, 740–788. [\[CrossRef\]](#)
- Grachev, P.Y.; Tabachinskiy, A.S.; Kanagavel, P. New Stator Construction and Simulation of High-Efficiency Wind Turbine Generators. *IEEE Trans. Ind. Appl.* **2020**, *56*, 1389–1396. [\[CrossRef\]](#)
- Liu, N.; Gao, H.; Xu, B.; Wu, Y. Comparative analysis of wind field fault characteristics of squirrel-cage wind farms and direct-drive wind farms. In Proceedings of the 7th Asia Conference on Power and Electrical Engineering (ACPEE), Hangzhou, China, 15–17 April 2022.
- Silva, E.O.; Vanço, W.E.; Guimarães, G.C. A Technical and Economic Project Analysis of Asynchronous Technology in Distributed Generation Using Methane Gas From Pig Farms. *IEEE Access* **2020**, *8*, 36140–36153. [\[CrossRef\]](#)
- Brennen and, M.B.; Abbondanti, A. Static Exciters for Induction Generators. *IEEE Trans. Ind. Appl.* **1977**, *IA-13*, 422–428. [\[CrossRef\]](#)
- Wagner, C.F. Self-Excitation of Induction Motors. *Trans. Am. Inst. Electr. Eng.* **1939**, *58*, 47–51. [\[CrossRef\]](#)
- Sanjenbam, C.D.; Shah, P.; Singh, B. Standalone Pico-Hydro Battery Integrated Universal Power Active Filter for PQ Improvement. In Proceedings of the IEEE 2nd International Conference on Smart Technologies for Power, Energy and Control (STPEC), Bilaspur, India, 19–22 December 2021.
- Esquivel-Sancho, L.M.; Pereira-Arroyo, R.; Muñoz-Arias, M. Voltage Regulation for a Self-Excited Induction Generator. In Proceedings of the 60th IEEE Conference on Decision and Control (CDC), Austin, TX, USA, 14–17 December 2021.
- Satpathy, A.S.; Kastha, D.; Kishore, N.K. Vienna Rectifier-Fed Squirrel Cage Induction Generator Based Stand-Alone Wind Energy Conversion System. *IEEE Trans. Power Electron.* **2021**, *36*, 10186–10198. [\[CrossRef\]](#)
- Chatterjee, J.K.; Perumal, B.V.; Gopu, N.R. Analysis of operation of a self-excited induction generator with generalized impedance controller. *IEEE Trans. Energy Convers.* **2007**, *22*, 307–315. [\[CrossRef\]](#)
- Górski, D.A.; Iwański, G. Asynchronous Grid Connection of a Cage Induction Generator Excited by a Power Electronic Converter. *IEEE Trans. Energy Convers.* **2021**, *36*, 63–70. [\[CrossRef\]](#)
- De Mello, F.P.; Feltes, J.W.; Hannett, L.N.; White, J.C. Application of Induction Generators in Power Systems. *IEEE Trans. Power Appar. Syst.* **1982**, *PAS-101*, 3385–3393. [\[CrossRef\]](#)
- Vanço, W.E.; Silva, F.B.; Monteiro, J.R.B.A.; de Oliveira, C.M.R.; Gomes, L.C. Theoretical-Experimental Analysis of the Induction Generator in the Use of Distributed Generation. *IEEE Lat. Am. Trans.* **2021**, *19*, 396–403. [\[CrossRef\]](#)
- Abdin, E.S.; Xu, W. Control design and dynamic performance analysis of a wind turbine-induction generator unit. *IEEE Trans. Energy Convers.* **2000**, *15*, 91–96. [\[CrossRef\]](#)
- Strzelecki, R.; Benysek, G. *Power Electronics in Smart Electrical Energy Networks*; Power Systems; Springer: Berlin/Heidelberg, Germany, 2008.
- Moreno-Muñoz, A. *Power Quality Mitigation Technologies in a Distributed Environment*; Power Systems; Springer: Berlin/Heidelberg, Germany, 2007.
- Nguyen, A.T.; Lee, D.C. Sensorless Control of Variable-Speed SCIG Wind Energy Conversion Systems Based on Rotor Flux Estimation Using ROGI-FLL. *IEEE J. Emerg. Sel. Top. Power Electron.* **2022**, *10*, 7786–7796. [\[CrossRef\]](#)
- Mishra, R.; Saha, T.K. Virtual Power-Based Control for Operation and Grid Synchronization of Induction Generator. *IEEE Syst. J.* **2021**, *15*, 2168–2175. [\[CrossRef\]](#)
- Hazra, S.; Bhattacharya, S. An Active Filter-Enabled Power Architecture for Oscillating Wave Energy Generation. *IEEE J. Emerg. Sel. Top. Power Electron.* **2017**, *5*, 723–734. [\[CrossRef\]](#)
- Wiik, J.A.; Fonstelién, O.J.; Shimada, R. A MERS type series FACTS controller for low voltage ride through of induction generators in wind farms. In Proceedings of the 13th European Conference on Power Electronics and Applications, Barcelona, Spain, 8–10 September 2009.

25. Guazzelli, P.R.U.; dos Santos, S.T.A.; de Castro, A.G.; de Andrade Pereira, W.C.; de Oliveira, C.M.R.; de Almeida Monteiro, J.R.B.; de Aguiar, M.L. Decoupled Predictive Current Control With Duty-Cycle Optimization of a Grid-Tied Nine-Switch Converter Applied to an Induction Generator. *IEEE Trans. Power Electron.* **2022**, *37*, 2778–2789. [[CrossRef](#)]
26. Sikorski, A.; Kuźma, A. Cooperation of induction squirrel-cage generator with grid connected AC/DC/AC converter. *Bull. Pol. Acad. Sci.* **2009**, *57*, 317–322. [[CrossRef](#)]
27. Béchir, B.; Faouzi, B.; Gasmı, M. Wind energy conversion system with full-scale power converter and squirrel cage induction generator. *Int. J. Phys. Sci.* **2012**, *6093*, 7–6104.
28. Rodriguez, J.; Cortes, P. *Predictive Control of Power Converters and Electrical Drives; Power Energy and Industry Applications*; Wiley-IEEE Press: Hoboken, NJ, USA, 2012.
29. Kot, R.; Rolak, M.; Malinowski, M. Comparison of maximum peak Power cracking algorithms for a small wind turbine. *Math. Comput. Simul.* **2013**, *91*, 29–40. [[CrossRef](#)]
30. Serhoud, H.; Benattous, D. Maximal Wind Energy Tracing of Brushless Doubly-Fed Generator under Flux Oriented Vector Control. *Int. J. Renew. Energy Res.* **2012**, *2*, 243–249.
31. Koutroulis, E.; Kalaitzakis, K. Design of Maximum Power Tracking System for Wind-Energy-Conversion Applications. *IEEE Trans. Ind. Electron.* **2006**, *53*, 486–494. [[CrossRef](#)]
32. Aouzellag, D.; Ghedams, K.; Berkouk, E.M. Power Control of a Variable Speed Wind Turbine Driving an DFIG. *Renew. Energ. Power Qual. J.* **2006**, *1*, 31–35. [[CrossRef](#)]
33. El-Sousy, F.F.M.; Orabi, M.; Godah, H. Maximum Power Point Tracking Control Scheme for Grid Connected Variable Speed Wind Driven Self-Excited Induction Generator. *J. Power Electron.* **2006**, *6*, 52–66.
34. Agarwal, V.; Aggarwal, R.K.; Patidar, P.; Patki, C. A Novel Scheme for Rapid Tracking of Maximum Power Point in Wind Energy Generation Systems. *IEEE Trans. Energy Convers.* **2010**, *25*, 228–236. [[CrossRef](#)]
35. Kouro, S.; Malinowski, M.; Gopakumar, K.; Pou, J.; Franquelo, L.G.; Wu, B.; Rodriguez, J.; Pérez, M.A.; Leon, J.I. Recent advances and industrial applications of multilevel converters. *IEEE Trans. Ind. Electron.* **2010**, *57*, 2553–2580. [[CrossRef](#)]
36. Martinez-Rodrigo, F.; Ramirez, D.; de Pablo, S.; Herrero-de Lucas, L.C. Connection System for Small and Medium-Size Wind Generators through the Integration in an MMC and NLC Modulation. *Energies* **2021**, *14*, 2681. [[CrossRef](#)]
37. Strzelecki, R.; Szczepankowski, P.; Parchomiuk, M.; Grabarek, M. Two-way converter 4L-DC with active voltage control in intermediate circuit. *Przegląd Elektrotechniczny* **2012**, *88*, 12–17. (In Polish)
38. Wojciechowski, D. Control system for parallel active filter with coupling LCL circuit. *Przegląd Elektrotechniczny* **2010**, *86*, 65–70. (In Polish)
39. Holmes, D.G.; Martin, D.A. Implementation of a Direct Digital Predictive Current Controller for Single and Three Phase Voltage Source Inverter, IAS 96. In Proceedings of the 1996 IEEE Industry Applications Conference Thirty-First IAS Annual Meeting, San Diego, CA, USA, 6–10 October 1996.
40. Kouro, S.; Perez, M.A.; Rodriguez, J.; Llor, A.M.; Young, H.A. Model Predictive Control: MPC's Role in the Evolution of Power Electronics. *IEEE Ind. Electron. Mag.* **2015**, *9*, 8–21. [[CrossRef](#)]
41. Falkowski, P.; Sikorski, A. Finite Control Set Model Predictive Control for Grid-Connected AC—DC Converters with LCL Filter. *IEEE Trans. Ind. Electron.* **2018**, *65*, 2844–2852. [[CrossRef](#)]
42. Hu, J.; Shan, Y.; Guerrero, J.M.; Ioinovici, A.; Chan, K.W.; Rodriguez, J. Model predictive control of microgrids—An overview. *Renew. Sustain. Energy Rev.* **2021**, *136*, 110422. [[CrossRef](#)]
43. Wojciechowski, D.; Strzelecki, R. Predictive Control of Active Filter System with LCL Coupling Circuit. In Proceedings of the 2010 International Power Electronics Conference, Sapporo, Japan, 21–24 June 2010.
44. Kasproicz, A. Voltage and frequency stabilisation system of self-excited induction generator. *Przegląd Elektrotechniczny* **2016**, *92*, 296–301. (In Polish)
45. Akagi, H.; Kanazawa, Y.; Nabae, A. Generalized theory of the instantaneous reactive power in three-phase circuits. *Conf. Rec. IEEJ-IPEC* **1983**, *103*, 1375–1386.
46. Akagi, H.; Watanabe, E.H.; Aredes, M. *Instantaneous Power Theory and Applications to Power Conditioning; Power Energy and Industry Applications*; Wiley-IEEE Press: Hoboken, NJ, USA, 2007.
47. Souza, H.; Neves, F.; Cavalcanti, M.; Bueno, E.; Rizo, M. Frequency Adaptive Phase-Sequence Separation Method Based on a Generalized Delayed Signal Cancellation Method. In Proceedings of the 2009 IEEE Energy Conversion Congress and Exposition, San Jose, CA, USA, 20–24 September 2009.
48. Wang, Y.F.; Li, Y.W. Grid Synchronization PLL Based on Cascaded Delayed Signal Cancellation. *IEEE Trans. Power Electron.* **2011**, *26*, 1987–1997. [[CrossRef](#)]
49. Wang, Y.F.; Li, Y.W. Analysis and Digital Implementation of Cascaded Delayed-Signal-Cancellation PLL. *IEEE Trans. Power Electron.* **2011**, *26*, 1067–1080. [[CrossRef](#)]
50. Bobrowska-Rafał, M.; Rafał, K.; Jasiński, M.; Kaźmierkowski, M.P. Grid synchronization and symmetrical components extraction with PLL algorithm for grid connected power electronic converters—A review. *Bull. Pol. Acad. Sci.* **2011**, *59*, 485–497. [[CrossRef](#)]



51. Wang, Y.F.; Li, Y.W. Three-Phase Cascaded Delayed Signal Cancellation PLL for Fast Selective Harmonic Detection. *IEEE Trans. Ind. Electron.* **2013**, *60*, 1452–1463. [[CrossRef](#)]
52. Malinowski, M.; Milczarek, A.; Kot, R.; Goryca, Z.; Szuster, J.T. Optimized Energy-Conversion Systems for Small Wind Turbines: Renewable energy sources in modern distributed power generation systems. *IEEE Power Electron. Mag.* **2015**, *2*, 16–30. [[CrossRef](#)]

**Disclaimer/Publisher’s Note:** The statements, opinions and data contained in all publications are solely those of the individual author(s) and contributor(s) and not of MDPI and/or the editor(s). MDPI and/or the editor(s) disclaim responsibility for any injury to people or property resulting from any ideas, methods, instructions or products referred to in the content.